Modeling microperforated panels and permeable membranes for a room acoustic solver with plane-wave enriched FEM

Mukae, Shunichi
Okuzono, Takeshi
Tamaru, Kanako
Sakagami, Kimihiro

(Citation)
Applied Acoustics,185:108383

(Issue Date)
2022-01-01

(Resource Type)
journal article

(Version)
Accepted Manuscript

Modeling microperforated panels and permeable membranes for a room acoustic solver with plane-wave enriched FEM

Shunichi Mukae[a,1] Takeshi Okuzono[a] Kanako Tamaru[a] and Kimihiro Sakagami[a]

[a]*Environmental Acoustic Laboratory, Department of Architecture, Graduate School of Engineering, Kobe University, 1-1, Rokkodai, Nada, Kobe 657-8501, Japan*

Abstract

Plane-wave-enriched finite element method (FEM), an efficient wave-based prediction method, uses shape functions incorporating a set of plane waves propagating in various directions to enhance the sound field approximation capability. The method can be an efficient wave-based acoustic solver for room acoustic simulations because it can simulate wave phenomena in rooms accurately with markedly fewer finite elements in spatial discretization than those used for standard FEM. However, several aspects remain to be addressed before its use for practical room acoustic simulations. Accurate sound absorber modelings able to address their frequency and incident angle dependence of absorption characteristics present extremely important issues. This paper presents a proposal of a method of implementing an extended-reaction model of microperforated panel (MPP) and permeable membrane (PM) sound absorbers into a room acoustic solver with plane-wave-enriched FEM. First, we demonstrate the validity of the proposed method in comparison with theoretical values in which impedance tube problems including three sound absorbers composed of MPP and PM are used. Then, the effectiveness over standard FEM is demonstrated via 2D real-scale office problems with the three MPP-PM sound absorbers.

[1]Corresponding author. Tel./fax: +81 78 803 6577.
E-mail address: okuzono@port.kobe-u.ac.jp (T. Okuzono).

Keywords: Microperforated panel, Partition of unity finite element method, Permeable membrane, Plane wave enrichment, q-refinement, Room acoustics

---

Nomenclature

(ξ, η) Local coordinate system

(x, y) Cartesian coordinate system

α_0 Normal incidence sound absorption coefficient

$\boldsymbol{A}$ Nodal amplitude vector constructed from element amplitude vector $\boldsymbol{A}_\mathrm{e}$

$\boldsymbol{C}$ Global dissipation matrix constructed from element dissipation matrix $\boldsymbol{C}_\mathrm{e}$

$\boldsymbol{D}$ Global MPP matrix constructed from element MPP matrix $\boldsymbol{D}_\mathrm{e}$

$\boldsymbol{K}$ Global stiffness matrix constructed from element stiffness matrix $\boldsymbol{K}_\mathrm{e}$

$\boldsymbol{L}$ Global PM matrix constructed from element PM matrix $\boldsymbol{L}_\mathrm{e}$

$\boldsymbol{M}$ Global mass matrix constructed from element mass matrix $\boldsymbol{M}_\mathrm{e}$

$\boldsymbol{P}$ New shape function vector

$\boldsymbol{P}_\mathrm{a}$, $\boldsymbol{P}_\mathrm{b}$ New shape function vector for MPP element and PM element

$\boldsymbol{Q}$ External force vector constructed from element external force vector $\boldsymbol{Q}_\mathrm{e}$

Δp Sound pressure difference between both sides of MPP or PM

η Dynamic viscosity of air

$\frac{\partial p}{\partial n}$ Normal pressure gradient

Γ_0 Rigid boundary

$\Gamma_{\mathrm{e,m}}$ MPP element having two boundary surfaces $\Gamma_{\mathrm{e,m_a}}$ and $\Gamma_{\mathrm{e,m_b}}$

$\Gamma_{e,p}$ PM element having two boundary surfaces Γ_{e,p_a} and Γ_{e,p_b}

Γ_v, Γ_{v_e} Vibration boundary and vibration boundary for element

Γ_z, Γ_{z_e} Absorbing boundary and absorbing boundary for element

$\int_\Gamma \cdot d\Gamma$, $\int_{\Gamma_e} \cdot d\Gamma_e$ Boundary integral and boundary integral in an element

$\int_\Omega \cdot d\Omega$, $\int_{\Omega_e} \cdot d\Omega_e$ Domain integral and domain integral in an element

λ Wavelength in air

∇ Gradient of variable

Ω Closed sound field

ω Angular frequency

Ω_e Air element

ϕ Weight function

π Circular constant

ρ_0 Air density

j Imaginary unit $\sqrt{-1}$

θ_l Propagation angle of plane wave in polar coordinate system

A_i^l Amplitude of plane waves propagating in a direction θ_l

C Constant to calculate q

c_0 Speed of sound in air

f Frequency

h_{max} Maximum element length

k_0 Wavenumber in air

L Thickness of air cavity

$L_{\mathrm{fem}}(f, i)$ SPLs calculated using PW-FEM and standard FEM in a receiver i at frequency f

$L_{\mathrm{ref}}(f, i)$ Reference SPL value calculated using fourth-order accurate FEM in a receiver i at frequency f

$L_{\mathrm{rms}}(f)$ RMS error at frequency f with respect to spatial distribution of SPL

M_{m}, M_{p} Surface density of MPP and PM

n Number of node in a finite element

N_i Shape function

n_{g} Number of integration points in high-order Gauss–Legendre rule

N_{node} Number of nodes in FE mesh

N_{p} Number of receiving point

n_{w} Ratio of wavelength to maximum length of element

P New shape function defined as the product of shape function N_i and plane wave with unit amplitude $\mathrm{e}^{\mathrm{j}k_0(x\cos\theta_l + y\sin\theta_l)}$

p Sound pressure

p_i Nodal sound pressure in a finite element

q Number of plane waves for enrichment

r, ωm Resistance and reactance in Maa's impedance model

R_{m} Flow resistance of PM

t Time

t_{p}, d, ε Panel thickness, hole diameter, perforation ratio of MPP

v_{f} Particle velocity on rigid MPP surface

v_{m}, v_{n} Vibration velocity of limp MPP and on vibration boundary surface

Y_{m}, Y_{p} Transfer admittance of MPP and PM

$Z(\mathrm{M})$ Acoustic impedance at point M

Z_{m} Acoustic impedance of MPP

z_{n} Specific acoustic impedance ratio on absorbing surface

1. Introduction

Room acoustic solvers using wave-based numerical methods such as finite element method (FEM) can simulate wave phenomena inside rooms accurately with physically reliable modeling. By virtue of recent advances in computer technology, the applicability of wave-based solvers to room acoustic simulations is progressing rapidly in both frequency and time domains [1, 2, 3, 4]. In general, FEM [5, 6, 7, 8] and the boundary element method [9, 10] are standard selections for room acoustic simulations in the frequency domain, whereas recent time-domain room acoustic simulations use various numerical methods such as the finite-difference time-domain method [11, 12, 13, 14, 15], time-domain FEM [2, 16, 17, 18], finite-volume time-domain method [19, 20], pseudospectral time-domain method [21, 22], discontinuous Galerkin FEM [23, 24, 25, 26], and the adaptive rectangular decomposition method [27, 28]. However, wave-based room acoustic predictions are still computationally expensive in practical applications. It is therefore desirable to develop methods that are more efficient and thereby to enhance their applicability further. Moreover, accurate room acoustic simulations require the usage of extended-reaction boundary modelings by which the frequency and incident-angle dependence of various sound absorbers can be incorporated properly in simulations[7, 9, 18, 26, 29, 30]. For time-domain room acoustic simulations, incorporating a local-reaction frequency-dependent impedance boundary is still a challenging task because of the inherent difficulty of addressing frequency-dependent quantities in a time domain. Many studies [25, 28, 30, 31] have been undertaken to implement a frequency-dependent impedance boundary efficiently for time-domain acoustic simulations. For accurate room acoustics simulations, a recent study presented an useful method to ascertain the surface impedance of various sound absorbers from octave-band absorption coefficients [32]. Toward constructing an efficient wave-based room acoustic solver, this paper presents a proposal for extended-reaction models of two sound absorbers for room

acoustic simulations in frequency domain using Partition of Unity Finite Element Method (PUFEM) [33].

The PUFEM is a highly accurate numerical method incorporating a general solution of governing equations into shape functions. In earlier works [34, 35, 36] acoustic PUFEMs and PU-based methods were formulated to solve the Helmholtz equation efficiently. For instance, a PUFEM formulation using plane wave enrichment uses a set of plane waves propagating in various directions at each node in an element to enhance the approximation capability of sound fields. Herein, we define the formulation as plane-wave-enriched FEM. In doing so, sound fields are approximated up to high frequencies under a single coarse mesh using a refinement approach. The refinement, called q-refinement, adds a set of plane waves at nodal points gradually with increasing frequency. Consequently, the plane-wave-enriched FEM achieves marked reduction of degrees of freedom (DOF) compared to the standard FEM. A recent report [37] described two room acoustic problems in which the DOF reduction reaches $\mathcal{O}(10^{-2})$, at least against the standard FEM. Therefore, plane-wave-enriched FEM can be an efficient room acoustic solver. However, the room acoustic solver using plane-wave-enriched FEM remains under development. Various aspects remain to be studied before its practical application. The development of extended-reaction models of sound absorbers is one such aspect.

Typically, to control acoustics inside rooms, sound absorbers of two types are used: porous absorbers and Helmholtz resonators. Two earlier works [38, 39] present implementation of an equivalent fluid model and a poroelastic material model, which are used as extended-reaction models for porous absorbers, in plane-wave-enriched FEM analyses. With these implementation techniques, sound absorption effects of porous materials such as glass wools and carpets can be adequately incorporated in room acoustic simulations. However, for other sound-absorbing materials such as microperforated panels and permeable membranes, extended-reaction models must be developed to accommodate their sound absorption effects adequately.

Microperforated panels (MPPs), thin panels with submillimeter perforations below a 1% perforation ratio, are made of various materials such as metals, wood, and plastics. The classical sound absorbers using MPPs are single-leaf and double-leaf MPP absorbers, respectively using an MPP or two MPPs in front of an air cavity to form Helmholtz type sound absorption [40, 41]. Permeable membranes (PM) are air-permeable thin fabrics made from various natural and chemical fibers [42, 43]. Absorption curtains

and suspended ceilings are examples of PM absorbers that have a porous type sound absorption mechanism. Actually, MPP absorbers and PM absorbers are attractive in terms of both sound absorptivity and aesthetic perspective, which are necessary for room acoustic design. Therefore, many MPP and PM absorbers have been proposed [44, 45, 46, 47, 48] and applied to create comfortable acoustic spaces according to room uses and environments [49].

These analyses were conducted to present a method of incorporating MPP and PM absorbers into a room acoustic solver using plane-wave-enriched FEM, and to demonstrate their applicability. The presented extended-reaction model can deal adequately with the frequency-dependence and incident-angle dependence of both absorbers. The remainder of this paper is organized as follows. Section 2 presents incorporation methods based on interior absorbing boundary conditions. In Section 3, the validity of the incorporation method will be shown via impedance tube problems including three sound absorbers composed of MPPs and PMs. Section 4 demonstrates the effectiveness of the developed room acoustic solver using plane-wave-enriched FEM against the standard FEM via 2D room acoustic problems including three MPP-PM absorbers.

2. Theory

The explanation of this section incorporates MPP and PM via interior impedance boundary conditions into the discretized matrix equation of the plane-wave-enriched FEM. The incorporation method [29] has been used in standard FEM, in which both MPP and PM are expressed as transfer admittance.

2.1. Interior impedance boundary conditions for MPP

Figure 1(a) presents the theoretical model of MPP and PM having respective transfer admittance Y_{m} and Y_{p}. In Fig. 1, $\Delta p(= p_{\mathrm{a}} - p_{\mathrm{b}})$ represents the sound pressure difference between both sides of an MPP or a PM, Z_{m} denotes the MPP acoustic impedance, R_{p} stands for the PM flow resistance, M_{m} denotes the MPP surface density, M_{p} expresses the PM surface density, j is an imaginary unit, and ω represents the angular frequency. Figure 1(b) shows an FE model of MPP and PM, where $\Gamma_{\mathrm{e,m}}$ and $\Gamma_{\mathrm{e,p}}$ respectively represent the MPP element and the PM element, having two boundary surfaces $\Gamma_{\mathrm{e,m_a}}$ and $\Gamma_{\mathrm{e,m_b}}$ for MPP and $\Gamma_{\mathrm{e,p_a}}$ and $\Gamma_{\mathrm{e,p_b}}$ for PM. In addition, Ω_{e} is the air element. $\mathbf{n}_{\mathrm{a}}$ and $\mathbf{n}_{\mathrm{b}}$ are the normal vectors at the boundary surface.

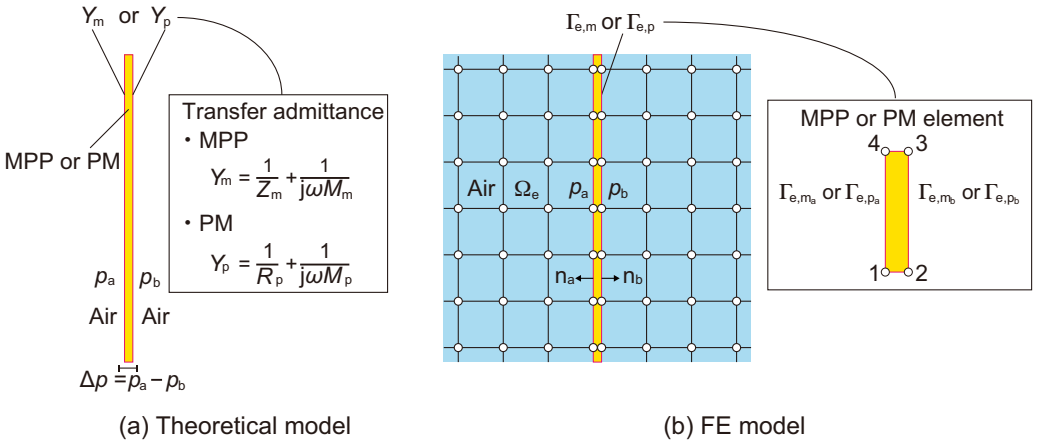

Figure 1: Theoretical model of MPP or PM and its spatially discretized FE model.

An MPP is assumed as a limp material with surface density M_{m} and vibration velocity v_{m}. The equation of motion can be expressed as

$$M_{\mathrm{m}} \frac{\partial v_{\mathrm{m}}}{\partial t} = \Delta p. \tag{1}$$

The sound absorption effect of MPP is expressed by its acoustic impedance Z_{m} as

$$Z_{\mathrm{m}} = \frac{\Delta p}{v_{\mathrm{f}}}, \tag{2}$$

where Z_{m} stands for the acoustic impedance of rigid MPP and v_{f} denotes the particle velocity on the rigid MPP surface. For this paper, we use the following simple impedance model presented by Maa [40] as

$$Z_{\mathrm{m}} = \frac{r + \mathrm{j}\omega m}{\varepsilon}, \tag{3}$$

with

$$r = \frac{32\eta t_{\mathrm{p}}}{d^2} \left(\sqrt{1 + \frac{K^2}{32}} + \frac{\sqrt{2}}{8} K \frac{d}{t_{\mathrm{p}}} \right), \tag{4}$$

$$\omega m = \rho_0 \omega t_{\mathrm{p}} \left(1 + \frac{1}{\sqrt{9 + \frac{K^2}{2}}} + 0.85 \frac{d}{t_{\mathrm{p}}} \right), \tag{5}$$

$$K = d\sqrt{\frac{\omega\rho_0}{4\eta}}, \tag{6}$$

where ρ_0, t_p, d, ε, and η respectively represent the air density, panel thickness, hole diameter, perforation ratio, and dynamic viscosity of air (=17.9 μPa s). Furthermore, the transfer admittance Y_m of MPP is defined with the two Eqs. (1) and (2) as

$$Y_\mathrm{m} = \frac{1}{Z_\mathrm{m}} + \frac{1}{\mathrm{j}\omega M_\mathrm{m}}. \tag{7}$$

Transfer admittance Y_m is imposed on the surfaces $\Gamma_{\mathrm{e,m_a}}$ and $\Gamma_{\mathrm{e,m_b}}$ via interior absorbing boundary conditions, which are described below.

$$\frac{\partial p}{\partial n} = \begin{cases} -\mathrm{j}\omega\rho_0 Y_\mathrm{m}\Delta p & \text{on } \Gamma_{\mathrm{e,m_a}}, \\ \mathrm{j}\omega\rho_0 Y_\mathrm{m}\Delta p & \text{on } \Gamma_{\mathrm{e,m_b}}. \end{cases} \tag{8}$$

Because the interior absorbing boundary conditions are imposed on both sides of material surfaces, it can model the backing structure in sound absorbers, having the capability of dealing accurately with the incident-angle dependence of absorbers.

2.2. Interior impedance boundary conditions for PM

We assume a PM as a limp material with no tension. The air permeability is expressed by flow resistance R_p. Similarly to the MPP, the transfer admittance Y_p of PM is defined as

$$Y_\mathrm{p} = \frac{1}{R_\mathrm{p}} + \frac{1}{\mathrm{j}\omega M_\mathrm{p}}. \tag{9}$$

With the transfer admittance above, the interior absorbing boundary conditions for PMs are given as

$$\frac{\partial p}{\partial n} = \begin{cases} -\mathrm{j}\omega\rho_0 Y_\mathrm{p}\Delta p & \text{on } \Gamma_{\mathrm{e,p_a}}, \\ \mathrm{j}\omega\rho_0 Y_\mathrm{p}\Delta p & \text{on } \Gamma_{\mathrm{e,p_b}}. \end{cases} \tag{10}$$

2.3. PUFEM discretization of a sound field including MPP and PM

Room acoustic problems generally solve the following Helmholtz equation in terms of sound pressure p for predicting sound propagation in a closed sound field Ω.

$$\nabla^2 p + k_0^2 p = 0 \quad \text{in } \Omega, \tag{11}$$

where k_0 stands for the wavenumber in air. For boundary conditions, we consider five boundaries: The interior absorbing boundary condition for MPP, the interior absorbing boundary condition for PM, the rigid boundary condition Γ_0, the vibration boundary condition Γ_v, and the absorbing boundary condition Γ_z. The latter three boundary conditions are described as

$$\frac{\partial p}{\partial n} = \begin{cases} 0 & \text{on } \Gamma_0 \\ -\mathrm{j}\omega\rho_0 v_\mathrm{n} & \text{on } \Gamma_\mathrm{v} \\ -\mathrm{j}\omega k_0 \frac{1}{z_\mathrm{n}} p & \text{on } \Gamma_\mathrm{z} \end{cases}, \tag{12}$$

where v_n and z_n respectively denote the vibration velocity and the specific acoustic impedance ratio. The weak form for plane-wave-enriched FEM is given as

$$\int_\Omega (-\nabla\phi\nabla p + k_0^2\phi p)\mathrm{d}\Omega + \int_\Gamma \phi\frac{\partial p}{\partial n}\mathrm{d}\Gamma = 0, \tag{13}$$

where ϕ is the arbitrary weight function.

In a standard FEM, sound pressure at an arbitrary point $p(x, y)$ within element Ω_e is approximated as

$$p(x, y) = \sum_{i=1}^{n} N_i(\xi, \eta)p_i, \tag{14}$$

where $N_i(\xi, \eta)$ and p_i respectively represent the shape function with two-dimensional local coordinate (ξ, η) and nodal sound pressure in finite elements. In the plane-wave-enriched FEM, the plane wave, which is a general solution of the Helmholtz equation, is incorporated into the shape function via the partition of unity property. Figure 2 presents plane-wave-enriched discretization of space Ω and q-refinement approach where the space is discretized with four-node quadrilateral elements. As the figure shows, for two-dimensional analysis, p_i is expressed as a set of plane waves propagating in various directions as

$$p_i = \sum_{l=1}^{q} \mathrm{e}^{\mathrm{j}k_0(x\cos\theta_l + y\sin\theta_l)} A_i^l, \tag{15}$$

where q, θ_l, and A_i^l respectively represent the number of plane waves, the angles of plane waves and the amplitude of plane waves propagating in a direction θ_l. Figure 2 portrays examples of plane-wave-enrichment for q=4, 8,

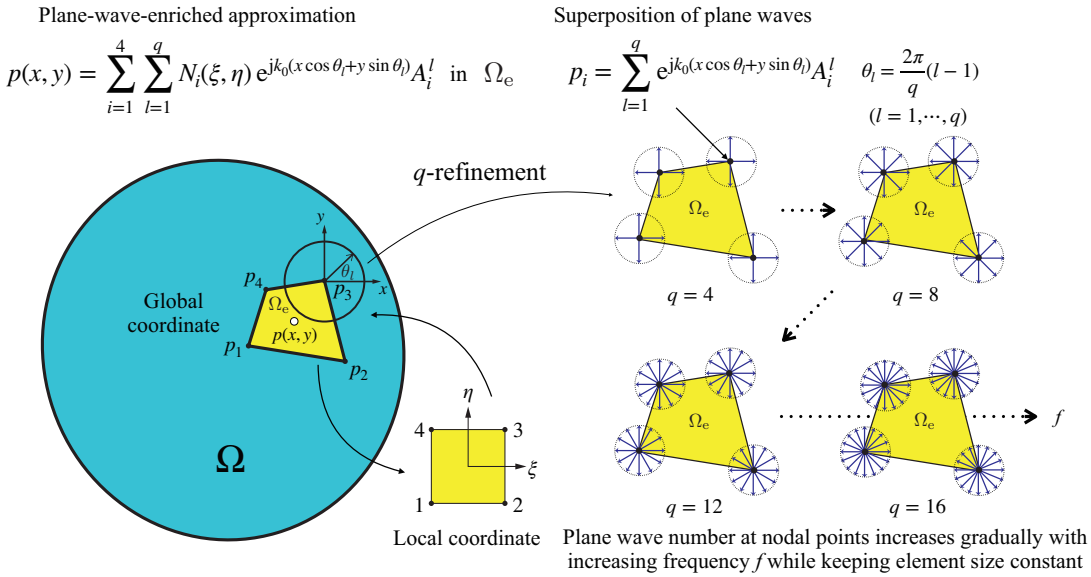

Figure 2: Plane-wave-enriched finite element discretization and q-refinement.

12 and 16, where an unit circle is evenly discretized as $\theta_l = \frac{2\pi(l-1)}{q}$. Inserting Eq. (15) into Eq. (14), $p(x,y)$ in an element Ω_e is approximated as

$$p(x,y) = \sum_{i=1}^{n}\sum_{l=1}^{q} N_i(\xi,\eta) e^{jk_0(x\cos\theta_l + y\sin\theta_l)} A_i^l. \tag{16}$$

For the readers' convenience Table 1 gives the shape function N_i for four-node quadrilateral elements. Equation (16) can be described simply as

$$p(x,y) = \sum_{i=1}^{n}\sum_{l=1}^{q} P_{(i-1)q+l}(\xi,\eta) A_i^l, \tag{17}$$

with definition of a new shape function P, which is defined as the product of shape function N_i and plane wave $e^{jk_0(x\cos\theta_l+y\sin\theta_l)}$, i.e., $P_{(i-1)q+l}(\xi,\eta) = N_i(\xi,\eta)e^{jk_0(x\cos\theta_l+y\sin\theta_l)}$. The analysis in the present paper designates approximation in Eq. (16) or Eq. (17) as plane-wave-enriched finite elements (FEs). As shown in Figure 2 the plane-wave-enriched FEs discretization uses q-refinement in which plane wave number q at nodal points increases gradually with increasing frequency f while maintaining the element size as constant. The method of increasing the plane wave number is explained

Table 1: Shape functions of four-node quadrilateral elements

	i=1	i=2	i=3	i=4
N_i	$\frac{1}{4}(1-\xi)(1-\eta)$	$\frac{1}{4}(1+\xi)(1-\eta)$	$\frac{1}{4}(1+\xi)(1+\eta)$	$\frac{1}{4}(1-\xi)(1+\eta)$
$\frac{\partial N_i}{\partial \xi}$	$-\frac{1}{4}(1-\eta)$	$\frac{1}{4}(1-\eta)$	$\frac{1}{4}(1+\eta)$	$-\frac{1}{4}(1+\eta)$
$\frac{\partial N_i}{\partial \eta}$	$-\frac{1}{4}(1-\xi)$	$-\frac{1}{4}(1+\xi)$	$\frac{1}{4}(1+\xi)$	$\frac{1}{4}(1-\xi)$

later. Then the weak form of the Helmholtz equation in Eq. (13) is discretized spatially using the plane-wave-enriched FEs together with the five boundary conditions. The discretized matrix equation can be expressed as

$$\sum_{\mathrm{e}}[\boldsymbol{K}_{\mathrm{e}}-k_0^2\boldsymbol{M}_{\mathrm{e}}+\mathrm{j}k_0\boldsymbol{C}_{\mathrm{e}}+\rho_0\boldsymbol{D}_{\mathrm{e}}+\rho_0\boldsymbol{L}_{\mathrm{e}}]\boldsymbol{A}_{\mathrm{e}}=\sum_{\mathrm{e}}[-\mathrm{j}\omega\rho_0\boldsymbol{Q}_{\mathrm{e}}], \tag{18}$$

where $\boldsymbol{K}_{\mathrm{e}}$, $\boldsymbol{M}_{\mathrm{e}}$, $\boldsymbol{C}_{\mathrm{e}}$, $\boldsymbol{D}_{\mathrm{e}}$, and $\boldsymbol{L}_{\mathrm{e}}$ respectively represent the element stiffness matrix, the element mass matrix, the element dissipation matrix, the element MPP matrix, and the element PM matrix. $\boldsymbol{A}_{\mathrm{e}}$ and $\boldsymbol{Q}_{\mathrm{e}}$ are, respectively, the element amplitude vector and the element external force vector. Finally, we obtain the following linear system of equations expressed as

$$[\boldsymbol{K}-k_0^2\boldsymbol{M}+\mathrm{j}k_0\boldsymbol{C}+\rho_0\boldsymbol{D}+\rho_0\boldsymbol{L}]\boldsymbol{A}=-\mathrm{j}\omega\rho_0\boldsymbol{Q}, \tag{19}$$

where $\boldsymbol{K}$, $\boldsymbol{M}$, and $\boldsymbol{C}$ respectively represent the global stiffness matrix, the global mass matrix, and the global dissipation matrix. Both $\boldsymbol{D}$ and $\boldsymbol{L}$ respectively denote the global matrix constructed from the element MPP matrix and element PM matrix. In addition, $\boldsymbol{A}$ and $\boldsymbol{Q}$ respectively denote the nodal amplitude vector and the external force vector. With the shape function vector $\boldsymbol{P}$ constructed from the new shape function $P_{(i-1)q+l}(\xi,\eta)$, i.e., $\boldsymbol{P}=[P_1,P_2,\cdots,P_{(i-1)q+l},\cdots,P_{4q}]$, the global matrices and vectors are described as

$$\boldsymbol{K}=\sum_{\mathrm{e}}\boldsymbol{K}_{\mathrm{e}}=\sum_{\mathrm{e}}\int_{\Omega_{\mathrm{e}}}\nabla\boldsymbol{P}^{\mathrm{T}}\nabla\boldsymbol{P}\mathrm{d}\Omega_{\mathrm{e}}, \tag{20}$$

$$\boldsymbol{M}=\sum_{\mathrm{e}}\boldsymbol{M}_{\mathrm{e}}=\sum_{\mathrm{e}}\int_{\Omega_{\mathrm{e}}}\boldsymbol{P}^{\mathrm{T}}\boldsymbol{P}\mathrm{d}\Omega_{\mathrm{e}}, \tag{21}$$

$$\boldsymbol{C}=\sum_{\mathrm{e}}\boldsymbol{C}_{\mathrm{e}}=\sum_{\mathrm{e}}\frac{1}{z_{\mathrm{n}}}\int_{\Gamma_{\mathrm{e,z}}}\boldsymbol{P}^{\mathrm{T}}\boldsymbol{P}\mathrm{d}\Gamma_{\mathrm{e}}, \tag{22}$$

Table 2: Shape functions of four-node MPP and PM elements, in which absorbing surfaces of elements respectively consist of nodes i = 1–4 and i = 2-3, as presented in Fig. 1(b).

	i=1	i=2	i=3	i=4
$N_{\mathrm{a},i}$	$\frac{1}{2}(1-\xi)$	0	0	$\frac{1}{2}(1+\xi)$
$N_{\mathrm{b},i}$	0	$\frac{1}{2}(1-\xi)$	$\frac{1}{2}(1+\xi)$	0
$\frac{\partial N_{\mathrm{a},i}}{\partial \xi}$	$-\frac{1}{2}$	0	0	$\frac{1}{2}$
$\frac{\partial N_{\mathrm{b},i}}{\partial \xi}$	0	$-\frac{1}{2}$	$\frac{1}{2}$	0

$$\boldsymbol{D}=\sum_{\mathrm{e}}\boldsymbol{D}_{\mathrm{e}}=\sum_{\mathrm{e}}\mathrm{j}\omega Y_{\mathrm{m}}\int_{\Gamma_{\mathrm{e,m_{a,b}}}}(\boldsymbol{P}_{\mathrm{a}}^{\mathrm{T}}(\boldsymbol{P}_{\mathrm{a}}-\boldsymbol{P}_{\mathrm{b}}) -\boldsymbol{P}_{\mathrm{b}}^{\mathrm{T}}(\boldsymbol{P}_{\mathrm{a}}-\boldsymbol{P}_{\mathrm{b}}))\mathrm{d}\Gamma_{\mathrm{e}}, \tag{23}$$

$$\boldsymbol{L}=\sum_{\mathrm{e}}\boldsymbol{L}_{\mathrm{e}}=\sum_{\mathrm{e}}\mathrm{j}\omega Y_{\mathrm{p}}\int_{\Gamma_{\mathrm{e,p_{a,b}}}}(\boldsymbol{P}_{\mathrm{a}}^{\mathrm{T}}(\boldsymbol{P}_{\mathrm{a}}-\boldsymbol{P}_{\mathrm{b}}) -\boldsymbol{P}_{\mathrm{b}}^{\mathrm{T}}(\boldsymbol{P}_{\mathrm{a}}-\boldsymbol{P}_{\mathrm{b}}))\mathrm{d}\Gamma_{\mathrm{e}}, \tag{24}$$

$$\boldsymbol{Q}=\sum_{\mathrm{e}}\boldsymbol{Q}_{\mathrm{e}}=\sum_{\mathrm{e}}v_{\mathrm{n}}\int_{\Gamma_{\mathrm{e,v}}}\boldsymbol{P}^{\mathrm{T}}\mathrm{d}\Gamma_{\mathrm{e}}. \tag{25}$$

In the equations presented above, $\boldsymbol{P}_{\mathrm{a}}$ and $\boldsymbol{P}_{\mathrm{b}}$ respectively represent the new shape functions at nodes on $\Gamma_{\mathrm{e,m_a}}$ and $\Gamma_{\mathrm{e,m_b}}$ for the MPP element or $\Gamma_{\mathrm{e,p_a}}$ and $\Gamma_{\mathrm{e,p_b}}$ for the PM element. For plane-wave-enriched four-node quadrilateral MPP and PM elements used for this study, $\boldsymbol{P}_{\mathrm{a}}$ and $\boldsymbol{P}_{\mathrm{b}}$ respectively denote constructions using shape functions $N_{\mathrm{a},i}$ and $N_{\mathrm{b},i}$, which are presented in Table 1. Finally, sound pressures in the domain are calculable by substituting the amplitudes of plane waves A_i^l obtained from Eq. (19) into Eq. (16) or Eq. (17). For spatial discretization in the air domain, we used plane-wave-enriched four-node quadrilateral elements. Furthermore, for the absorbing boundary and vibration boundary, we applied plane-wave-enriched two-node line elements. The domain and boundary integrals appearing in element matrix construction are calculated using high-order Gauss–Legendre rules. In plane-wave-enriched FEM, the number of integration points n_{g} in the high-order Gauss–Legendre rules change according to the frequency and element sizes. We applied the following rule to ascertain the number of integration

points [37, 50] as

$$n_{\mathrm{g}} = \begin{cases} 10 & (n_{\mathrm{w}} < 1) \\ \mathrm{int}(10n_{\mathrm{w}} + 1) & (n_{\mathrm{w}} \geq 1) \end{cases}, \tag{26}$$

where n_{w} represents the ratio of wavelength λ to the maximum length of each element $h_{\max}(n_{\mathrm{w}} = h_{\max}/\lambda)$.

3. Validation with Impedance Tube Problems

To demonstrate the validity of the proposed implementation method of MPP and PM in a room acoustic solver with plane-wave-enriched FEM, we conducted numerical experiments based on the impedance tube method with the transfer function method to calculate the sound absorption characteristics of sound absorbers. We calculated the specific acoustic impedance ratio and the sound absorption coefficient of three sound absorbers, which are composed respectively of MPP and PM. Then they were compared respectively with the theoretical values using the transfer matrix method described in Appendix A at frequencies of 10 Hz to 8 kHz with a 1 Hz interval. The speed of sound c_0 and air density ρ_0 were assumed respectively as 340 m/s and 1.205 kg/m^3.

3.1. Numerical setup

Figure 3 presents an impedance tube model. Using this model, we calculated the sound absorption characteristics of three MPP-PM absorbers, as shown in Figs. 4(a)–(c): (a) a single-leaf MPP absorber, (b) a double-leaf MPP absorber, and (c) a PM-MPP absorber. We assumed that the MPP is made of an MS sheet and that the PM is made of glass cloth, each with the following material parameters: $M_{\mathrm{m}} = 1.13$ kg/m^2, $d = 0.5$ mm, $t_{\mathrm{p}} = 1$ mm, $\varepsilon = 0.77\%$ for MPP, and $M_{\mathrm{p}} = 0.205$ kg/m^2, $R_{\mathrm{p}} = 1200$ Pa s/m for PM.

The vibration velocity of 1.0 m/s was assigned on the surface in the tube inlet. The tube outlet boundary surface is perfectly rigid. For plane-wave-enriched FE analysis, we used the meshes shown as Figures 5(a) and 5(b), respectively, for the single-leaf absorber and the double-leaf absorbers. The element length in the x-direction is 0.2 m for the domain in front of the absorbers. The backing air cavity was discretized with 0.05 m or 0.1 m length elements in the x-direction. The length in y-direction is 0.01 m. However, for the standard FE analysis, we used a uniform mesh discretized with 0.005

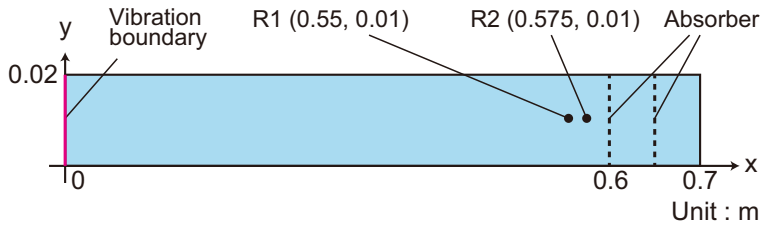

Figure 3: Impedance tube model for validation study.

m square elements having 8.5 elements per wavelength at the upper-limit frequency of 8 kHz. Two receiving points R1 and R2 were placed in front of the three sound absorbers, as in Fig 3. The plane waves q in the plane-wave-enriched FEs were two ($\theta_l = 0, \pi$) because the sound field was describable completely by the superposition of two plane waves propagating in opposite directions.

3.2. Results and discussion

Figures 6(a)–(c) present comparisons of the specific acoustic impedance ratio and normal incidence absorption coefficients of each absorber calculated using the theory, standard FEM, and plane-wave-enriched FEM. For all sound absorbers, the plane-wave-enriched FEM results showed excellent agreement with theoretical results, suggesting the validity of the proposed method. It is noteworthy that the plane-wave-enriched FEM produces quite accurate results compared to standard FEM without plane wave enrichment, even for the use of the coarse meshes, which were discretized with 4.65 times larger element sizes than the wavelength of the upper-limit frequency.

The FEM results in the impedance and the absorption coefficient showed markedly large discrepancies from the theory at frequencies higher than 4 kHz and 6 kHz, respectively. These discrepancies are attributable to the large dispersion error for the standard FEM. Actually, the numerical sound speed in the standard FEM becomes faster at higher frequencies under given mesh. The following section underscores the effectiveness of plane-wave-enriched FEM against standard FEM.

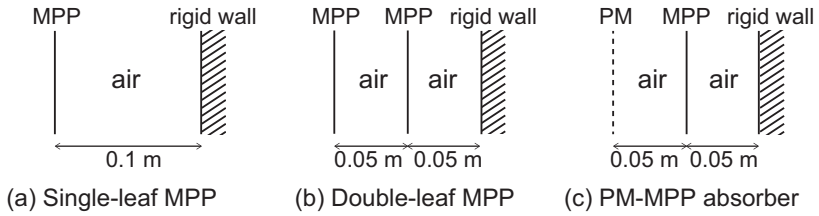

Figure 4: Three tested sound absorbers composed of MPP and PM: (a) Single-leaf MPP, (b) Double-leaf MPP, and (c) PM-MPP absorber.

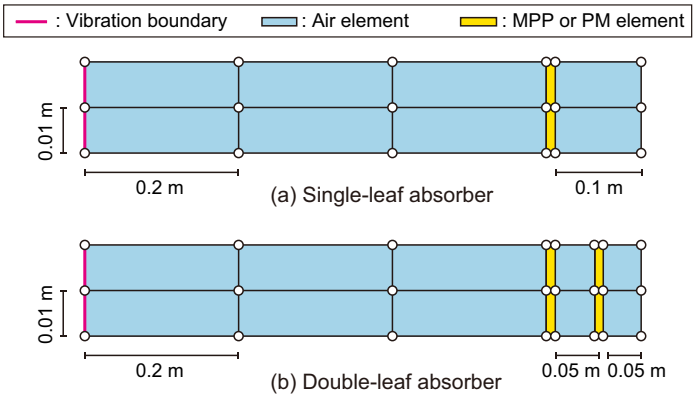

Figure 5: Meshes used for plane-enriched FE analysis: (a) Single-leaf absorber and (b) Double-leaf absorber.

4. Demonstration of Room Acoustic Solver Effectiveness with Plane-wave-enriched FEM against Standard FEM via 2D Room Acoustic Problems Including MPP-PM Sound Absorbers

As a practical benchmark case, we demonstrate the performance of the presented plane-wave-enriched FEM against a standard FEM through numerical experiments predicting a sound field in a 2D real-scale office room including three MPP-PM sound absorbers, which act as extend-reaction boundaries. As a demonstration, we show the accuracy of plane-wave-enriched FEM in comparison with the standard FEM without using plane-wave enrichment. The efficiency will be measured by the degree to which degrees of freedom can be reduced with the plane-wave-enriched solver.

4.1. Problem description and numerical setup

Figure 7 presents the 2D office model with a sound source S and 15 receivers R1–R15. The figure also includes the field-incidence sound absorption

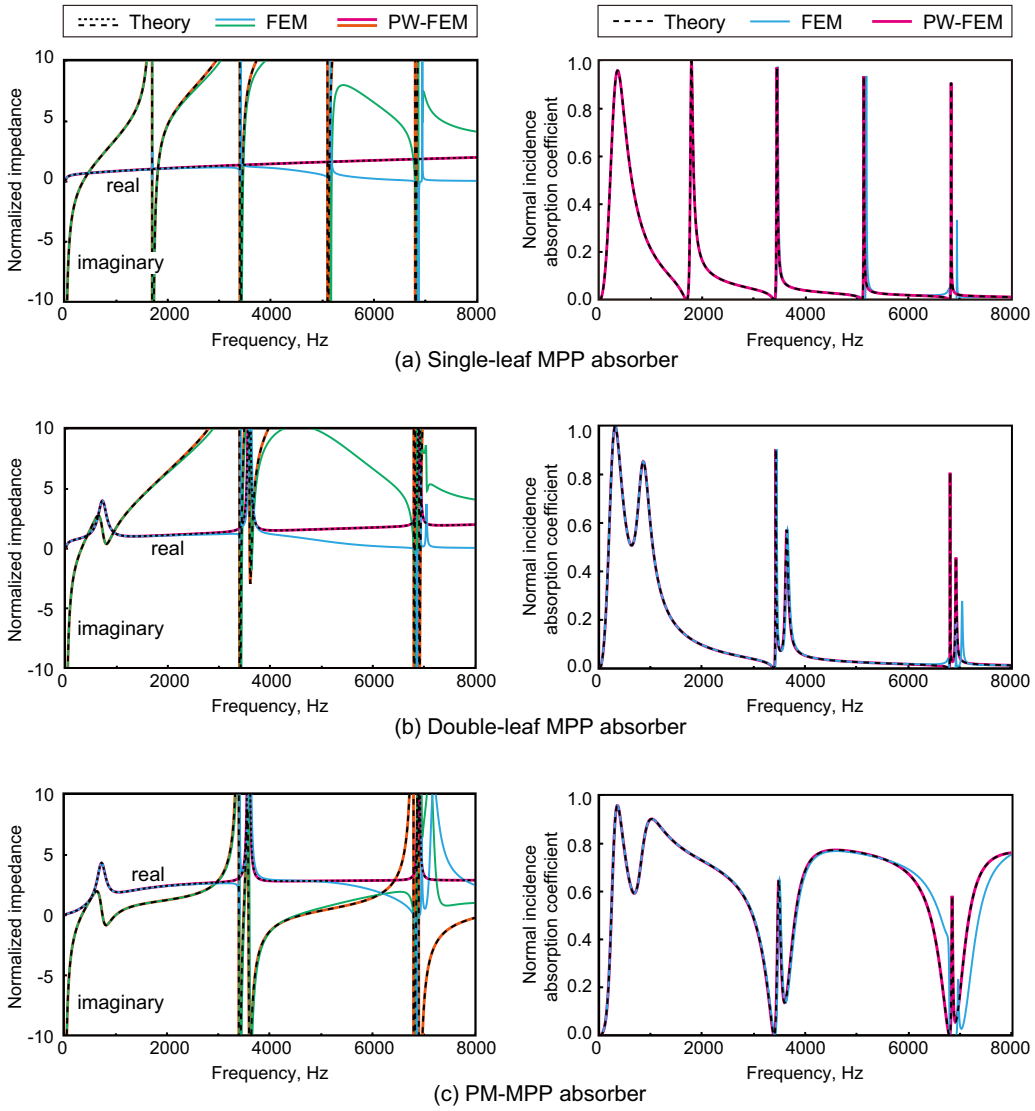

Figure 6: Specific acoustic impedance ratios and normal incidence absorption coefficients obtained using theory, standard FEM and plane-wave-enriched FEM (PW-FEM) for three sound absorbers (a), (b), and (c).

coefficient of the three tested MPP-PM absorbers: (a) a single-leaf MPP absorber, (b) a double-leaf MPP absorber, and (c) a PM-MPP absorber. The three tested absorbers have different sound absorption coefficients, as presented in the figure. We computed the sound fields generated by acoustic

emissions from a loudspeaker at 20 Hz – 2.5 kHz with a 1 Hz interval. The room has a domain Ω_1 with area of 39.92 m^2 and boundaries comprising a vibration boundary Γ_v assuming a loudspeaker, a weakly absorbing impedance boundary $\Gamma_{z,1}$, and an extended-reaction boundary $\Gamma_{z,2}$ of the three absorbers shown in Fig. 7. The weakly absorbing boundary $\Gamma_{z,1}$ has real valued impedance corresponding to the normal incidence absorption coefficient of α_0 = 0.05. The vibration boundary Γ_v has vibration velocity of v_n = 1.0 m/s. The speed of sound c_0 = 343.7 m/s and the air density ρ_0 =1.205 kg/m^3 were assumed. The problem has no analytical solution. Therefore, we used reference solutions using a fourth-order accurate FEM [29, 51] with sufficient fine meshes. The fourth-order accurate FEM uses dispersion-reduced finite elements for spatial discretization, in which dispersion reduction is achieved using the Gauss–Legendre integration rule with a modified integration point in the element matrix construction process. For plane-wave-enriched FE analysis, we used two coarse meshes Mesh 1 and Mesh 2 in domain Ω_1 with different spatial resolutions. Figures 8(a) and 8(b) respectively show Mesh 1 and Mesh 2, each discretized with plane-wave-enriched FEs having elements larger than the wavelength at the upper-limit frequency: Mesh 1 is a uniform mesh with element size of 0.2 m; Mesh 2 is a non-uniform mesh with element sizes in 0.2–0.4 m. They respectively use elements with 1.47 and 2.97 times greater length than the wavelength at the upper-limit frequency. However, we discretized using element sizes of 0.1 m in the domain of the single-leaf absorber and 0.05 m in the domains of the two double-leaf absorbers. For Mesh 1 and Mesh 2, the respective numbers of nodes, N_{node}, are 1,034 and 329 for the case with the single-leaf absorber, and 1,074 and 351 for the cases with the two double-leaf absorbers. We found the number of plane waves q for enrichment using the following equation [39] as

$$q = \text{round}\left[k_0 h_{\max} + C(k_0 h_{\max})^{\frac{1}{3}}\right], \tag{27}$$

where constant C controls the resulting accuracy. The constant C was set as 13 based on the results in our earlier report [37]. In this case, the DOF of Mesh 1 in the plane-wave-enriched FE analysis respectively change 6,204–38,258 for the single-leaf absorber and 6,444–39,738 for double-leaf absorbers. For Mesh 2, they change 2,303–17,437 for the single-leaf absorber and 2,457–18,603 for the double-leaf absorbers. The number of plane waves q respectively change in the ranges of 6–37 at frequencies 20 Hz – 2.5 kHz in Mesh 1 and 7–53 in Mesh 2. The number of integration points was found using Eq.

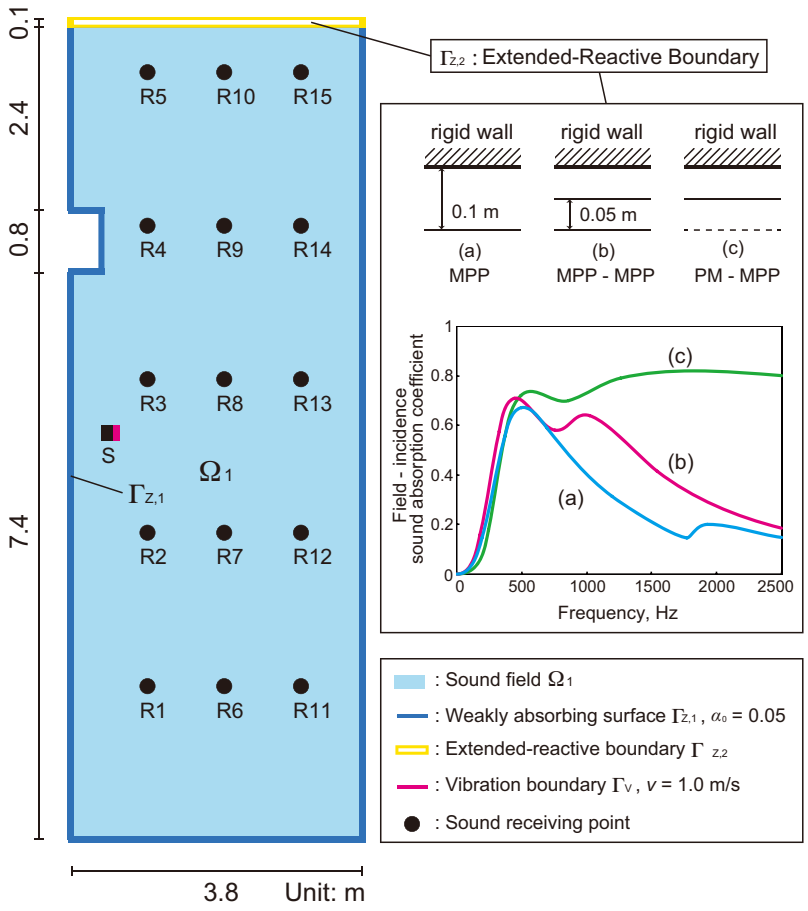

Figure 7: A 2D office model including three MPP-PM sound absorbers (a)–(c): Field-incidence sound absorption coefficients of three absorbers are also shown.

(24).

For the standard FE analysis, we used two finer meshes, Mesh 3 and Mesh 4, according to the analyzed frequencies. Mesh 3 is a uniform mesh discretized with 0.01 m square elements for frequencies of 20 Hz – 1.5 kHz. Mesh 4 is used for frequencies higher than 1.5 kHz, which is also a uniform mesh discretized with 0.005 m square elements. The DOF in Mesh 3 and Mesh 4 are, respectively, 404,911 and 1,615,821 for the single-leaf absorbers and 405,292 and 1,616,582 for the double-leaf absorbers. Mesh 3 and Mesh 4 have fine spatial resolution, the values of which are, respectively, 22 and 27 elements per wavelength at each upper-limit frequency. It is noteworthy

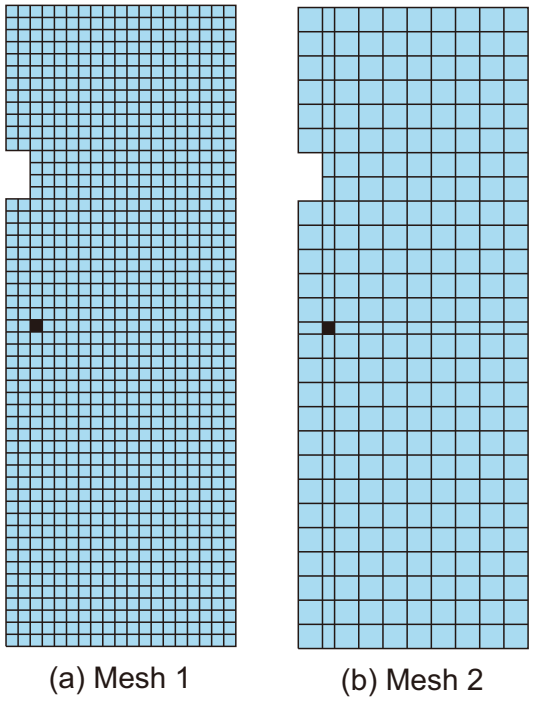

Figure 8: Meshes used for plane-wave-enriched FE analysis: (a) Mesh 1 with element length of 0.2 m and (b) Mesh 2 with element lengths of 0.2–0.4 m.

that these fine Mesh 3 and Mesh 4 were also used to calculate the reference solution with the fourth-order accurate FEM.

4.2. Method of accuracy evaluation

To evaluate the accuracy, we defined the RMS error $L_{\mathrm{rms}}(f)$ with respect to the spatial distribution of sound pressure level (SPL) as

$$L_{\mathrm{rms}}(f) = \sqrt{\frac{1}{N_{\mathrm{p}}} \sum_{i=1}^{N_{\mathrm{p}}} [L_{\mathrm{fem}}(f,i) - L_{\mathrm{ref}}(f,i)]^2}, \tag{28}$$

where $L_{\mathrm{fem}}(f,i)$ and $L_{\mathrm{ref}}(f,i)$ respectively represent the SPLs in a receiver i at frequency f calculated using the plane-wave-enriched FEM and the standard FEM, and the reference solution calculated using the fourth-order accurate FEM [29, 51] using Mesh 3 and Mesh 4. In addition, N_{p} represents the number of receiving points. To evaluate the error behavior easily, we applied 1/3 octave band averaging to the RMS error.

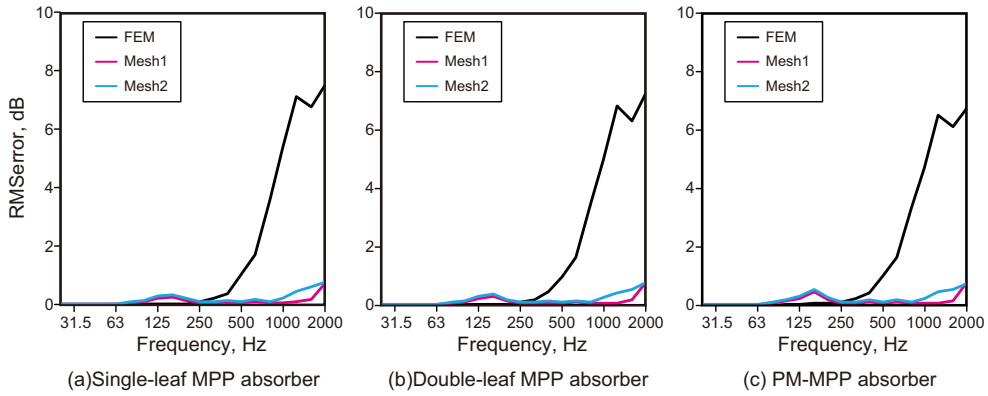

Figure 9: Comparisons of RMS errors among the plane-wave-enriched FEM (PW-FEM) with Mesh 1 and Mesh 2 and standard FEM: (a) single-leaf MPP, (b) double-leaf MPP, and (c) PM-MPP absorber.

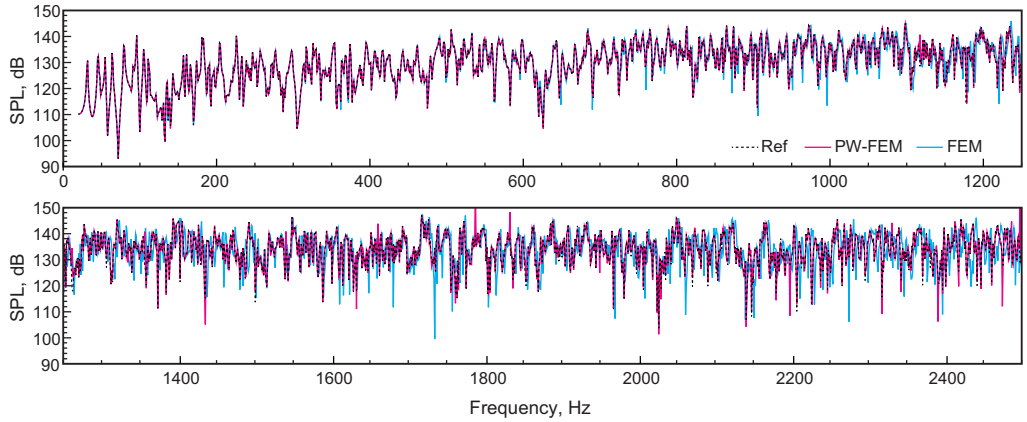

Figure 10: Comparison of frequency responses at R1 among the reference solution, the plane-wave-enriched FEM (PW-FEM) with Mesh 2, and standard FEM.

4.3. Results and discussion

Figures 9(a)–(c) respectively present comparisons of the 1/3 octave band averaging RMS errors in cases with three sound absorbers (a)–(c). They compare the RMS errors calculated using the plane-wave-enriched FEM with Mesh 1 and Mesh 2 against those calculated using the standard FEM. For all cases, the plane-wave-enriched FEM results obtained using Mesh 1 and Mesh 2 showed much better accuracy than the standard FEM results at frequencies higher than 315 Hz. Especially at frequencies higher than 1 kHz, the

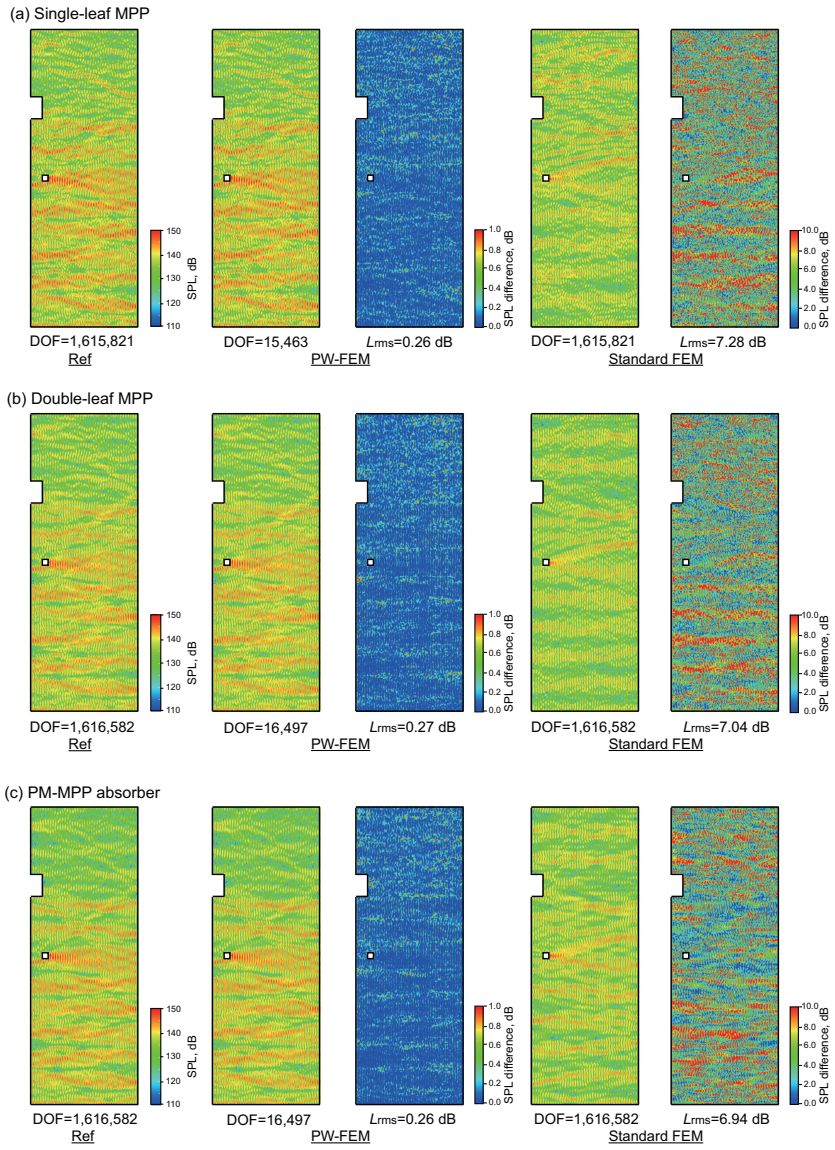

Figure 11: Comparisons of the SPL distribution inside room at 2 kHz among the reference solution, the plane-wave-enriched FEM (PW-FEM) with Mesh2 and the standard FEM and the SPL difference from the reference solution: (a) single-leaf MPP absorber, (b) double-leaf MPP absorber, and (c) PM-MPP absorber.

standard FEM results show RMS errors of more than 7 dB because of large dispersion errors. In contrast, the plane-wave-enriched FEM results show

RMS errors of around 0.7 dB at 2 kHz, even in the use of very coarse mesh of Mesh 2. The RMS errors of the plane-wave-enriched FEM are lower than 1 dB below 315 Hz. It is noteworthy that the reason for higher accuracy in the standard FEM below 315 Hz is simple. At that frequency, the used mesh has markedly high spatial resolution that exceeds 109 elements per wavelength. With Mesh 2, the DOF reduction reaches at least 1/100 compared to the standard FEM to obtain wideband frequency responses accurately. This result clearly demonstrated the effectiveness of using plane-wave-enriched FEs for room acoustic simulation including MPP-PM absorbers acting as extended-reaction boundaries. In addition, the plane-wave-enriched FEM requires no creation of FE meshes according to the frequencies, as in the standard FEM. The data capacity necessary to store the coordinates of nodes and the connectivity of elements becomes remarkably small. For those reasons, this method is attractive from the perspective of mesh construction.

As an example, Figure 10 portrays comparisons of frequency responses calculated using the plane-wave-enriched FEM with Mesh 2 and the standard FEM at a receiving point R1 against the reference solution. The standard FEM result presents marked differences because of large dispersion errors, despite the use of the mesh with spatial resolution of 27 elements per wavelength at 2.5 kHz. Because of the dispersion error, the sound speed for the standard FEM increases more than the exact values, especially for higher frequencies. Therefore, frequencies at which peaks and dips occur are shifted to higher frequencies. However, the plane-wave-enriched FEM shows a considerably better match to the reference solution at a wide frequency range. It is hardly seen for the given scale in the graph the frequency shift at which peaks and dips occur. This result suggests that the plane-wave-enriched FEs incorporating the general solution of Helmholtz equation can reduce the dispersion error considerably, even under the coarse mesh.

Finally, for cases with three sound absorbers, Figs. 11(a)–(c) show spatial distributions of SPLs at 2 kHz for the reference solution, the standard FEM, and the plane-wave-enriched FEM with Mesh 2, including a comparison of the spatial distribution of SPL difference from the reference solution for respective methods, and the SPLs in the plane-wave-enriched FEM calculated at the same nodes in the reference solution. The figure also includes the DOF and RMS error $L_{\mathrm{rms}}(f)$ for each method. For all cases presented in panels (a)–(c), the plane-wave-enriched FEM results showed excellent agreement with the SPL distributions of the reference solution with low error values of 0.26 dB or 0.27 dB. The standard FEM results show different SPL distri-

butions attributable to the dispersion error, as presented in the reference, although the mesh which was used has spatial resolution of 34 elements per wavelength at 2 kHz. Regarding sound absorption effects, the lower SPL around sound absorbers than those in the lower part of room for all cases by virtue of the installed sound absorbers is apparent. The effect is greatest for the PM-MPP sound absorber, which has the highest sound absorption, as shown in Fig. 5. Results of comparison for the spatial SPL distribution demonstrated clearly that the plane-wave-enriched FEM can resolve sound fields inside the room, including MPP-PM sound absorbers, accurately with considerably coarser mesh than that used for the standard FEM.

5. Conclusions

The present report described a study of a room acoustic solver with the plane-wave-enriched FEM to predict sound fields inside rooms including MPP and PM sound absorbers, which is an extended study of the authors' earlier work [37]. As the most notable contribution, we demonstrated how extended-reacting MPP and PM sound absorber are incorporated into plane-wave-enriched FEM. In the first part of this paper, we presented the method of incorporating MPP and PM via interior impedance boundary conditions, by which the backing structures of sound absorbers can be modeled. Consequently, it can function as an extended-reaction model for sound absorbers composed of MPP and PM. Then, the validity of the incorporation method is presented via impedance tube problems with three MPP-PM sound absorbers in comparison with theoretical values using the transfer matrix method. Finally, as more practical numerical examples, performance of the developed plane-wave-enriched FEM with the extended-reaction models is tested in comparison to the standard FEM for a 2D real-scale office problem including three MPP-PM sound absorbers. Numerical results revealed that the developed solver outperforms standard FEM to predict sound fields in rooms including extended-reaction MPP-PM absorbers over a wide frequency range with markedly fewer degrees of freedom and with markedly smaller dispersion errors, especially at higher frequencies.

Acknowledgments

This work was supported in part by JSPS KAKENHI Grant No. 20K04806. The computation was partly conducted using computer facilities at the Research Institute for Information Technology, Kyushu University.

Appendix A. Theoretical Sound Absorption Characteristics of Single and Double-leaf MPP Absorbers

In this Appendix, we present design theories of single and double-leaf MPP absorbers with the transfer matrix method.

Appendix A.1. Single-leaf absorber

Figure A.12(a) presents a model of the single-leaf MPP absorber with the air gap of thickness L_1. In the case of normal sound incidence, the acoustic impedance $Z(\mathrm{M}_2)$ at point M_2 is expressed as

$$Z(\mathrm{M}_2) = \rho_0 c_0 \frac{-\mathrm{j} Z(\mathrm{M}_1) \cot(k_0 L_1) + \rho_0 c_0}{Z(\mathrm{M}_1) - \mathrm{j}\rho_0 c_0 \cot(k_0 L_1)}, \tag{A.1}$$

where $Z(\mathrm{M}_1)$ represents the acoustic impedance at M_1. Because $Z(\mathrm{M}_1)$ in front of a rigid surface has an infinite value, $Z(\mathrm{M}_2)$ can be expressed further as

$$Z(\mathrm{M}_2) = -\mathrm{j}\rho_0 c_0 \cot(k_0 L_1). \tag{A.2}$$

The acoustic impedance $Z(\mathrm{M}_3)$ at M_3 is calculated with $Z(\mathrm{M}_2)$ and the transfer admittance Y_m of MPP as

$$Z(\mathrm{M}_3) = Y_\mathrm{m}^{-1} + Z(\mathrm{M}_2). \tag{A.3}$$

Finally, the specific acoustic impedance ratio z_n of the single-leaf absorber is calculated as

$$z_\mathrm{n} = \frac{Z(\mathrm{M}_3)}{\rho_0 c_0}. \tag{A.4}$$

The normal-incidence sound absorption coefficient α_0 is then calculated from

$$\alpha_0 = 1 - \left| \frac{z_\mathrm{n} - 1}{z_\mathrm{n} + 1} \right|^2. \tag{A.5}$$

Appendix A.2. Double-leaf absorber

Figure A.12(b) presents a model of the double-leaf MPP absorber or PM-MPP absorber. In normal sound incidence case, the acoustic impedance $Z(\mathrm{M}_4)$ at M_4 is expressed with $Z(\mathrm{M}_3)$ of Eq. (A.3) as

$$Z(\mathrm{M}_4) = \rho_0 c_0 \frac{-\mathrm{j} Z(\mathrm{M}_3) \cot(k_0 L_2) + \rho_0 c_0}{Z(\mathrm{M}_3) - \mathrm{j}\rho_0 c_0 \cot(k_0 L_2)}, \tag{A.6}$$

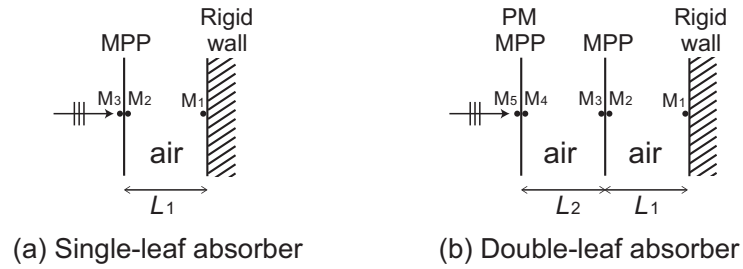

Figure A.12: Absorber models: (a) single-leaf absorber and (b) double-leaf absorber.

where L_2 represents the second air gap thickness. For the double-leaf MPP absorber, the acoustic impedance $Z(\mathrm{M}_5)$ at M_5 is calculated with $Z(\mathrm{M}_4)$ and Y_m as

$$Z(\mathrm{M}_5) = Y_\mathrm{m}^{-1} + Z(\mathrm{M}_4). \tag{A.7}$$

For the PM-MPP absorber, we can obtain $Z(\mathrm{M}_5)$ by substituting the transfer admittance Y_p of PM into Y_m in Eq. (A.7). Finally, z_n of the double-leaf absorber is expressed as

$$z_\mathrm{n} = \frac{Z(\mathrm{M}_5)}{\rho_0 c_0}. \tag{A.8}$$

The α_0 is then calculated using Eq. (A.5).

References

[1] Sakuma T, Sakamoto S, Otsuru T. Eds. Computational simulation in architectural and environmental acoustics – Methods and applications of wave-based computation –. Springer 2014.

[2] Okuzono T, Otsuru T, Tomiku R, Okamoto N. A finite element method using dispersion reduced spline elements for room acoustics simulation. Appl Acoust 2014;79:1–8.

[3] Botteldooren D. Finite-difference time-domain simulation of low-frequency room acoustics problems. J Acoust Soc Am 1995;98(6):3302–08.

[4] Otsuru T, Okamoto N, Okuzono T, Sueyoshi T. Applications of large-scale finite element sound field analysis onto room acoustics. In Proceedings of the 19th International Congress on Acoustics, Madrid, Spain, 2–7 September 2007.

[5] Okamoto N, Tomiku R, Otsuru T, Yasuda Y. Numerical analysis of large-scale sound fields using iterative methods part II: Application of Krylov subspace methods to finite element analysis. J Comput Acoust 2007;15:473–93.

[6] Aretz M, Vorländer M. Combined wave and ray based room acoustic simulations of audio systems in car passenger compartments, Part II: Comparison of simulations and measurements. Appl Acoust 2014;76:52–65.

[7] Okuzono T, Sakagami K. A frequency domain finite element solver for acoustic simulations of 3D rooms with microperforated panel absorbers. Appl Acoust 2018;129:1–12.

[8] Hoshi K, Hanyu T, Okuozno T, Sakagami K, Yairi M, Harada S, Takahashi S, Ueda Y. Implementation experiment of a honeycomb-backed MPP sound absorber in a meeting room. Appl Acoust 2020;157:107000.

[9] Yasuda Y, Ueno S, Kadota M, Sekine H. Applicability of locally reacting boundary conditions to porous material layer backed by rigid wall: Wave-based numerical study in non-diffuse sound field with unevenly distributed sound absorbing surfaces. Appl Acoust 2016;113:45–57.

[10] Yasuda Y, Saito K, Sekine H. Effects of the convergence tolerance of iterative methods used in the boundary element method on the calculation results of sound fields in rooms. Appl Acoust 2020;157:106997.

[11] Sakamoto S. Phase-error analysis of high-order finite-difference time-domain scheme and its influence on calculation results of impulse response in closed sound field. Acoust Sci and Tech 2007;28(5):295–309.

[12] Kowalczyk K, Walstijn M. Formulation of locally reacting surfaces in FDTD/K-DWM modelling of acoustic spaces. Acta Acust United Acta 2008;94:891–906.

[13] Kowalczyk K, Van Walstijn M. Room Acoustics Simulation Using 3-D Compact Explicit FDTD Schemes. IEEE Trans Audio Speech Lang Process 2010;19:4–46.

[14] Sakamoto S, Nagatomo H, Ushiyama A, Tachibana H. Calculation of impulse responses and acoustic parameters in a hall by the finite-difference time-domain method. Acoust Sci and Tech 2008;29(4):256–65.

[15] Hamilton B, Bilbao S. FDTD methods for 3-D room acoustics simulation with high-order accuracy in space and time. IEEE Trans Audio Speech Lang Process 2017;25:2112–24.

[16] Okuzono T, Otsuru T, Tomiku R, Okamoto N. Fundamental accuracy of time domain finite element method for sound field analysis of rooms. Appl Acoust 2010;71(10):940–6.

[17] Okuzono T, Yoshida T, Sakagami K, Otsuru T. An explicit time-domain finite element method for room acoustics simulations: Comparison of the performance with implicit methods. Appl Acoust 2016;104:76–84.

[18] Okuzono T, Shimizu N, Sakagami K. Predicting absorption characteristics of single-leaf permeable membrane absorbers using finite element method in a time domain. Appl Acoust 2019;151:172–82.

[19] Bilbao S. Modeling of Complex Geometries and Boundary Conditions in Finite Difference/Finite Volume Time Domain Room Acoustics Simulation. IEEE Trans. Audio Speech Lang Process 2013;21:1524–33.

[20] Bilbao S, Hamilton B, Botts J, Savioja L. Finite volume time domain room acoustics simulation under general impedance boundary conditions. IEEE Trans Audio Speech Lang Process 2016;24:161–73.

[21] Hornikx M, Hak C, Wenmaekers R. Acoustic modelling of sports halls, two case studies. J Build Perform Simul 2015;8:26–38.

[22] Hornikx M, Krijnen T, van Harten L. openPTSD: The open source pseudo-spectral time-domain method for acoustic propagation. Comput Phys Communications 2016;203:298–308.

[23] Simonaho SP, Lähivaara T, Huttunen T. Modeling of acoustic wave propagation in time-domain using the discontinuous Galerkin method – A comparison with measurements. Appl Acoust 2012;73:173–83.

[24] Wang H, Sihar I, Pagán Muñoz R, Hornikx M. Room acoustics modelling in the time-domain with the nodal discontinuous Galerkin method. J Acoust Soc Am 2019;145:2650–63.

[25] Wang H, Hornikx M. Time-domain impedance boundary condition modeling with the discontinuous Galerkin method for room acoustics simulations. J Acoust Soc Am 2020;147:2534–46.

[26] Pind F, Jeong CH, Hesthaven JS, Engsig-Karup AP, Strømann-Andersen J. A phenomenological extended-reaction boundary model for time-domain wave-based acoustic simulations under sparse reflection conditions using a wave splitting method. Appl Acoust 2021;172:107596.

[27] Mehra R, Raghuvanshi N, Savioja L, Lin MC, Manocha D. An efficient GPU-based time domain solver for the acoustic wave equation. Appl Acoust 2012;73:83–94.

[28] Rabisse K, Ducourneau J, Faiz A, Trompette N. Numerical modelling of sound propagation in rooms bounded by walls with rectangular irregularities and frequency-dependent impedance. J Sound Vib 2019;440:291–314.

[29] Okuzono T, Sakagami K. A finite-element formulation for room acoustics simulation with microperforated panel sound absorbing structures: Verification with electro-acoustical equivalent circuit theory and wave theory. Appl Acoust 2015;95:20–26.

[30] Toyoda M, Eto D. Prediction of microperforated panel absorbers using the finite-difference time-domain method. Wave Motion 2019;86:110–24.

[31] Yoshida T, Okuzono T, Sakagami K. Implementation of a frequency-dependent impedance boundary model into a room acoustic solver with time-domain finite element method. Acoust Sci and Technol 2020;41:819–22.

[32] Mondet B, Brunskog J, Jeong CH, Rindel JH. From absorption to impedance: Enhancing boundary conditions in room acoustic simulations. Appl Acoust 2020;157:106884.

[33] Melenk JM, Babuška I. Partition of unity finite element method: Basic theory and applications. Comput Methods Appl Mech Eng 1996;139:289–314.

[34] Laghrouche O, Mohamed MS. Locally enriched finite elements for the Helmholtz equation in two dimensions. Comput Struct 2010;88:469–1473.

[35] Mohamed MS, Laghrouche O, El-Kacimi A. Some numerical aspects of the PUFEM for efficient solution of 2D Helmholtz problems. Comput Struct 2010;88:1484–91.

[36] Diwan GC, Mohamed MS. Pollution studies for high order isogeometric analysis and finite element for acoustic problems. Comput Methods Appl Mech Engrg 2019;350:701–18.

[37] Okuzono T, Shadi Mohamed M, Sakagami K. Potential of room acoustic solver with plane-wave enriched finite element method. Appl Sci 2020;10:1969.

[38] Chazot JD, Nennig B, Perrey-Debain E. Performances of the partition of unity finite element method for the analysis of two-dimensional interior sound fields with absorbing materials. J Sound Vib 2013;332:1918–29.

[39] Chazot JD, Perrey-Debain E. The partition of unity finite element method for the simulation of waves in air and poroelastic media. J Acoust Soc Am 2014;135(2):724–33.

[40] Maa DY. Microperforated-panel wideband absorbers. Noise Control Eng J 1987;29(3):77–84.

[41] Maa DY. Potential of microperforated panel absorber. J Acoust Soc Am 1998;104(5):2861–6.

[42] Ingard KU. Sheet absorbers. Notes on Sound Absorption Technology. New York: Noise Control Foundation; 1994. Chap. 1, pp1-1–1-16.

[43] Pieren R. Sound absorption modeling of thin woven fabrics backed by an air cavity. Text Res J 2012;82(9):864–74.

[44] Liu W, Herrin DW, Bianchini E. Diffuse field sound absorption of microperforated panels with special backings. SAE Int J Veh Dyn Stab and NVH 2017;1(2):464–70.

[45] Cobo P, Simón F. Multiple-layer microperforated panels as sound absorbers in buildings: a review. Buildings 2019;9(2):53.

[46] Mosa Al, Putra A, Ramlan R, Prasetiyo I, Esraa AA. Theoretical model of absorption coefficient of an inhomogeneous MPP absorber with multi-cavity depths. Appl Acoust 2019;146:409–19.

[47] Sakagami K, Okuzono T, Suzuki H, Koyanagi N, Toyoda M. Application of paper folding technique to three-dimensional space sound absorber with permeable membrane: Case studies of trial productions. Int J Acoust and Vib 2020;25(2):243–47.

[48] Okuzono T, Uenishi K, Sakagami K. Experimental comparison of absorption characteristics of single-leaf permeable membrane absorbers with different backing air cavity designs. Noise Control Engr J 2020;68(3):237–45.

[49] Adams T. Sound Materials: A Compendium of Sound Absorbing Materials for Architecture and Design. New York: Frame Pub;2017.

[50] Tamaru K, Okuzono T, Mukae S, Sakagami K. Exploration of efficient numerical integration rule for wide-band room-acoustics simulations by plane-wave-enriched finite-element method. Acoust Sci and Technol (In print)

[51] Guddati MN, Yue B, Modified integration rules for reducing dispersion error in finite element methods. Comput Methods Appl Mech Engrg 2004;193:275–287.